

The properties of the clumpy torus and BLR in the polar-scattered Seyfert 1 galaxy ESO 323–G77 through X-ray absorption variability

G. Miniutti,^{1*} M. Sanfrutos,¹ T. Beuchert,² B. Agís-González,¹ A. L. Longinotti,³ E. Piconcelli,⁴ Y. Krongold,⁵ M. Guainazzi,³ S. Bianchi,⁶ G. Matt,⁶ and E. Jiménez-Bailón,⁵

¹Centro de Astrobiología (CSIC–INTA), Dep. de Astrofísica; ESAC, PO Box 78, Villanueva de la Cañada, E-28691 Madrid, Spain

²Dr. Remeis Sternwarte & ECAP, Universität Erlangen-Nürnberg, Sternwartstr. 7, 96049 Bamberg, Germany

³European Space Astronomy Centre of ESA P.O. Box 78, Villanueva de la Cañada, E-28691 Madrid, Spain

⁴Osservatorio Astronomico di Roma (INAF), Via Frascati 33. I-00040 Monteporzio Catone (Roma) Italy

⁵Instituto de Astronomía, Universidad Nacional Autónoma de México, Apdo. 70-264, Cd. Universitaria, México DF 04510, México

⁶Dipartimento di Matematica e Fisica, Università degli Studi Roma Tre, Via della Vasca Navale 84, 00146 Roma, Italy

22 November 2021

ABSTRACT

We report results from multi-epoch (2006–2013) X-ray observations of the polar-scattered Seyfert 1 galaxy ESO 323–G77. The source exhibits remarkable spectral variability from months to years timescales. The observed spectral variability is entirely due to variations of the column density of a neutral absorber towards the intrinsic nuclear continuum. The column density is generally Compton-thin ranging from a few times 10^{22} cm^{-2} to a few times 10^{23} cm^{-2} . However, one observation reveals a Compton-thick state with column density of the order of 1.5×10^{24} cm^{-2} . The observed variability offers a rare opportunity to study the properties of the X-ray absorber(s) in an active galaxy. We identify variable X-ray absorption from two different components, namely (i) a clumpy torus whose individual clumps have a density of $\leq 1.7 \times 10^8$ cm^{-3} and an average column density of $\sim 4 \times 10^{22}$ cm^{-2} , and (ii) the broad line region (BLR), comprising individual clouds with density of $0.1 - 8 \times 10^9$ cm^{-3} and column density of $10^{23} - 10^{24}$ cm^{-2} . The derived properties of the clumpy torus can also be used to estimate the torus half-opening angle, which is of the order of 47° . We also confirm the previously reported detection of two highly ionized warm absorbers with outflow velocities of $1000 - 4000$ km s^{-1} . The observed outflow velocities are consistent with the Keplerian/escape velocity at the BLR. Hence, the warm absorbers may be tentatively identified with the warm/hot inter-cloud medium which ensures that the BLR clouds are in pressure equilibrium with their surroundings. The BLR line-emitting clouds may well be the cold, dense clumps of this outflow, whose warm/hot phase is likely more homogeneous, as suggested by the lack of strong variability of the warm absorber(s) properties during our monitoring.

Key words: galaxies: active – X-rays: galaxies

1 INTRODUCTION

ESO 323–G77 ($z = 0.015$) is an optically bright ($m_V = 13.2$ mag) Seyfert 1 galaxy originally reported as an active galactic nucleus (AGN) by Fairall (1986). The nuclear spectrum indicates significant reddening with $A_V \simeq 1.04$ (Winkler 1992; Winkler et al. 1992), a property that is often observed in Seyfert 1 galaxies showing a high level of optical polarisation such as e.g. Mrk 231 and Fairall 51 (see Smith et al. 1995; Schmid et al. 2001). Indeed, Schmid et al. (2003) report the detection of high linear polarisation

in ESO 323–G77, ranging from $\sim 2.2\%$ at 8300 \AA to $\sim 7.5\%$ at 3600 \AA for the continuum. Similar amounts of polarisation are found for the broad emission lines. The position angle of the polarisation does not depend on wavelength, and it is found to be perpendicular to the orientation of the [O III] ionization cone of the galaxy. This suggests that ESO 323–G77 is observed at an intermediate inclination of $\sim 45^\circ$ with respect to the symmetry axis. Hence, ESO 323–G77 appears to be a borderline Seyfert 1 galaxy, seen at an inclination that is intermediate between the typical orientation of Seyfert 1 and Seyfert 2 galaxies, a viewing angle that is likely grazing the obscuring medium (the so-called torus of Unified models, Antonucci 1993).

* E-mail: gminiutti@cab.inta-csic.es

Table 1. Reference observation number, X-ray mission, detector, observation (starting) date, and net spectral exposure of all X-ray observations used in this work. The four Chandra observations have been merged, as no significant spectral variability was observed, see Section 2.

#	Mission	Detector	Date	Net exp. [ks]
1	XMM	EPIC pn	2006-02-07	~ 23
2	Swift	XRT PC	2006-06-28	~ 2
3	Swift	XRT PC	2006-08-17	~ 4
4	Swift	XRT PC	2006-09-14	~ 2
5	Chandra	MEG/HEG	2010-04-14	~ 46
6	Chandra	MEG/HEG	2010-04-19	~ 118
7	Chandra	MEG/HEG	2010-04-21	~ 60
8	Chandra	MEG/HEG	2010-04-24	~ 67
9	Suzaku	XIS(0,3)/PIN	2011-07-20	~ 88
10	XMM	EPIC pn	2013-01-17	~ 89

If this is the case, then one generally expects that more centrally-concentrated emitting regions (i.e. X-rays) will show a higher level of obscuration than more extended ones (e.g. optical and broad emission lines) as the latter (e.g. their far side) correspond to lower observer inclination than the former. Indeed, the optical extinction towards ESO 323-G77, as obtained by Winkler (1992) from the observed Balmer decrement, corresponds to a column density of $2.3 \times 10^{21} \text{ cm}^{-2}$ (e.g. Güver & Özel 2009), much lower than the X-ray-derived one, which is more than one order of magnitude higher (Jiménez-Bailón et al. 2008a), a clear case of mismatch between optical and X-ray absorption (see Maiolino et al. 2001). As such, ESO 323-G77 represents an ideal laboratory to study the properties of the torus and of its atmosphere in the X-ray band. Here we present results from multi-epoch X-ray observations of ESO 323-G77 in the 2006–2013 time-frame when the source has been observed with *XMM-Newton*, *Swift*, *Chandra*, and *Suzaku*. We focus here on the properties of the broadband X-ray continuum and on the X-ray absorption measurements. A (on-going) more detailed analysis of the high-resolution *Chandra* and *XMM-Newton* data devoted to the study of the warm absorber in ESO 323-G77 will be presented elsewhere (Sanfrutos et al. in preparation).

2 OBSERVATIONS

X-ray pointed observations of ESO 323-G77 have been performed with *XMM-Newton* (Jansen et al. 2001), *Swift* (Gehrels et al. 2004), *Chandra* (Weisskopf et al. 2000), and *Suzaku* (Mitsuda et al. 2007) since 2006. Details on the X-ray observations used in this work are given in Table 1. The data from the various missions and detectors have been reduced as standard using the dedicated software SAS v12.01 (*XMM-Newton*), CIAO v4.4 (*Chandra*), and HEASOFT v6.11 (*Swift* and *Suzaku*). Epoch- and position-dependent ancillary responses and redistribution matrices have been generated for each data set. Source products have been extracted from circular regions centred on the source, and background products have been generated from source-free regions close to the source. For simplicity, we only consider here EPIC pn spectra from *XMM-Newton*, although we have checked their consistency with the MOS data. The data from all EPIC cameras are in excellent agreement in the 0.5–10 keV band. On the other hand, as the MOS and pn data exhibit

some discrepancy below 0.5 keV, we make a conservative choice and we use the EPIC pn data in the 0.5–10 keV band. As for the *Suzaku* data, we merge the spectra from the front-illuminated CCD detectors XIS0 and XIS3 using the FTOOL ADDASCASPEC (unless otherwise specified). We also make use of the PIN data from the Suzaku HXD, which have been reduced with the dedicated FTOOL HXDSOXBPI. *Chandra* observed the source on 4 separate occasions (see Table 1) with the High-Energy-Transmission-Gratings (HETG). As our study focus on the continuum properties rather than on the superimposed spectral features, we are in principle interested in the higher signal-to-noise zeroth-order spectra. We have then extracted zeroth-order ACIS spectra from all observations. However, we find that the number of counts per frame in the innermost 3×3 pixel region exceeds the pile-up limit for 10 % pile-up in all observations. Hence, we use here the gratings spectra from the MEG and HEG detectors that are pile-up free. Moreover, after checking that there are no significant spectral differences between the individual *Chandra* observations (5, 6, 7, and 8 in Table 1), we merge all *Chandra* gratings spectra, to obtain one single ~ 10 days-averaged spectrum for each grating, representative of epoch 2010-04-14 to 2010-04-24 with a net exposure of ~ 291 ks. All CCD spectra are grouped to a minimum of 25 counts per background-subtracted energy bin, except the *Swift* XRT spectra that are grouped to a minimum of 5 counts per background-subtracted energy bin (we use the C-statistic for the spectral analysis of the *Swift* data). The *Chandra* MEG/HEG gratings spectra have been grouped to 30 channels per bin, and we checked that this grouping enables us to use the χ^2 statistic, as for all other data except the *Swift* XRT ones.

3 REMARKABLE X-RAY ABSORPTION VARIABILITY IN ESO 323-G77

The X-ray spectra of all observations reported in Table 1 are shown in Fig. 1. Each spectrum has been divided by the corresponding detector effective area to ease visual comparison. In the upper panel of Fig. 1, we show the full variability range that is observed in ESO 323-G77 from the higher quality observations in Table 1. Visual inspection of the spectra strongly suggests that the observed spectral variability is mostly associated with X-ray absorption changes. In the bottom panel of the same Fig. 1, we show the remaining *Swift* observations (2,3, and 4 in Table 1). The reason to show them in a different panel is twofold: firstly, the spectral shape during the *Swift* observations is almost coincident with that during the *XMM-Newton* ones (observations 2 and 10 are similar, as are observations 3, 4, and 1), so that the *Swift* data are shown separately for clarity; secondly, the *Swift* observations reveal the fastest variability event of the overall monitoring and are then worth special attention: as seen in the bottom panel of Fig. 1, observation 2 (black) is significantly more absorbed than observation 3 (red) which was performed ~ 2 months after.

3.1 Looking for a global spectral model

In order to define a global spectral model to be applied to all multi-epoch data, we first consider the two *XMM-Newton* observations 1 and 10 (see Table 1) which have the highest spectral quality. Hereafter, we consider the X-ray data in the 0.5–10 keV band, unless specified otherwise. Spectral analysis is performed using the XSPEC v12.7 software (Arnaud 1996). We start our analysis by defining a phenomenological, typical Seyfert 2-like spectral model

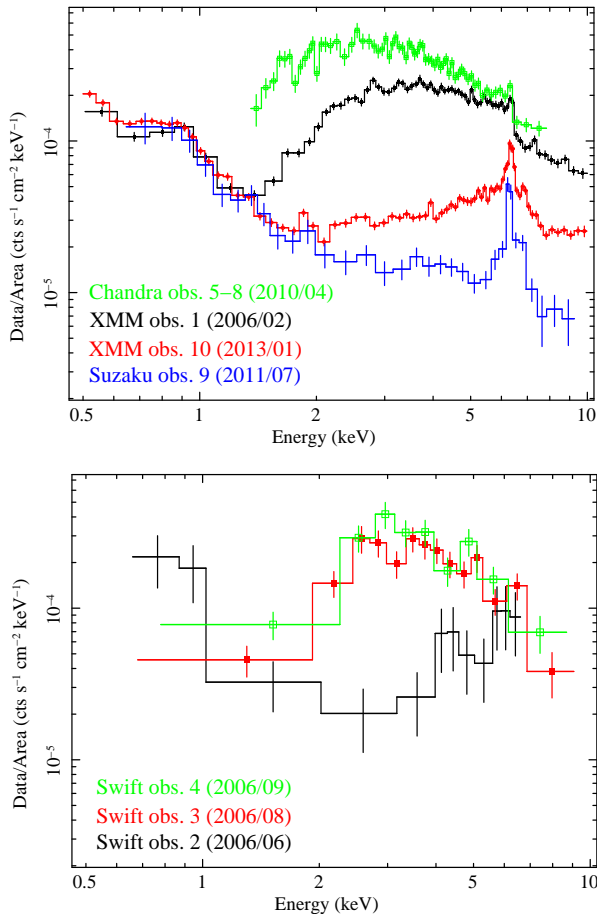


Figure 1. In the upper panel, we show the range of X–ray absorption variability in ESO 323–G77 as observed with *XMM–Newton*, *Chandra* (only the HEG data are shown for clarity), and *Suzaku* XIS. In the bottom panel we show the remaining *Swift* observations. All spectra have been rebinned for visual clarity.

comprising, besides Galactic absorption (applied to all components with $N_{\text{H}} = 7.98 \times 10^{20} \text{ cm}^{-2}$, see Kalberla et al. 2005), an intrinsic AGN power law nuclear continuum absorbed by a column density $N_{\text{H}}^{\text{nuc}}$ at the redshift of ESO 323–G77, a Gaussian emission line at rest–frame $\sim 6.4 \text{ keV}$ describing Fe K α emission, and a soft power–law which is only absorbed by the Galactic column density and represents the scattered component that is often associated with soft X–ray emission lines in the X–ray spectra of obscured AGN (e.g. Bianchi et al. 2005; Guainazzi & Bianchi 2007).

We force the continuum spectral index to be the same during both observations, deferring a discussion about this hypothesis to a later stage. As soft X–ray emission in obscured AGN likely originates in an extended region (possibly the narrow line region, see Bianchi, Guainazzi & Chiaberge 2006, as well as star–forming regions in the host galaxy), we force the soft power law normalisation to be the same at both epochs, and we also assume the same spectral index as that of the continuum. All the other parameters are allowed to vary independently. The model, which can be thought of as a rather typical Seyfert 2 spectral model, is not successful in describing the data resulting into $\chi^2 = 2343$ for 1450 degrees of freedom (dof). The data, spectral models, and data–to–model ratio for both observations are shown in Fig. 2. Important residuals are left in both observations around 0.9 keV pointing to the presence

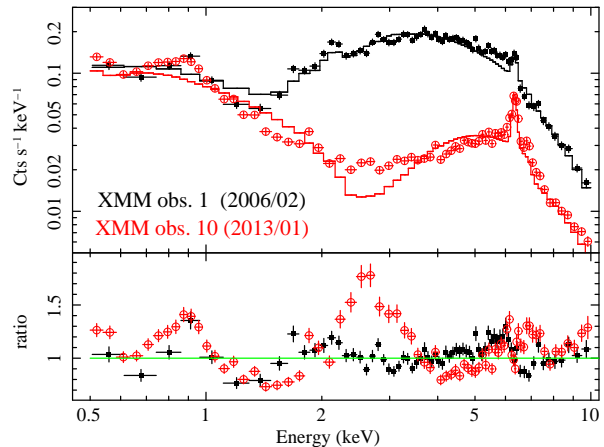


Figure 2. Data and models (upper panel), and data–to–model ratio (lower panel) for the *XMM–Newton* observations 1 and 10 using a typical Seyfert 2–like X–ray spectral model comprising an absorbed X–ray continuum, a narrow Fe K α emission line, and a soft X–ray power law component representing scattering/emission from distant material.

of a further soft (and constant) emission component. On the other hand, the two spectra differ significantly around 2–4 keV and in the Fe K band. In particular, the overall hard X–ray spectral shape of the more absorbed *XMM–Newton* observation 10 is not at all well described by our model.

As a first step, in order to account for the common residuals around 0.9 keV, we add an optically–thin plasma emission model, representing phenomenologically the soft X–ray contribution from either photo–ionized or collisionally–ionized gas (we use the APEC model in XSPEC, Smith et al. 2001). The normalisation is assumed to be the same at the two epochs, as the model is physically associated with extended emission. The fitting statistic improves significantly with $\chi^2 = 2154$ for 1448 dof for a plasma temperature of $kT^{(1)} \simeq 0.7 \text{ keV}$. Adding a second APEC component results in a better statistic with $\chi^2 = 2019$ for 1446 for a temperature of $kT^{(2)} \simeq 0.1 \text{ keV}$. These components account for the residuals below $\sim 2 \text{ keV}$ in Fig. 2 almost completely.

As already pointed out by Jiménez–Bailón et al. (2008a), the *XMM–Newton* observation 1 exhibits blueshifted absorption lines in the Fe K band that these authors model with two highly ionized outflowing absorbers. We then first add one ionized, outflowing absorber to our overall model using the ZXIPCF model (Reeves et al. 2008) in XSPEC assuming a covering fraction of unity. For simplicity, we force the same absorber parameters (column density and ionization) at both epochs, deferring the analysis of the ionized absorber variability to a later stage, once a satisfactory global spectral model is found. The fit improves significantly with $\chi^2 = 1936$ for 1443. Adding the second highly–ionized absorber identified by Jiménez–Bailón et al. (2008a) further improves the statistic to $\chi^2 = 1875$ for 1440. The absorbers are both highly–ionized ($\log \xi \simeq 3.4$ and $\simeq 4.1$) and outflowing with velocities of $1000 - 4000 \text{ km s}^{-1}$ (measured by letting the redshift parameter free to vary), in good agreement with previous results.

As for the emission components in the Fe K band, the Fe K emission is generally associated with an X–ray reflection continuum. We then remove the Gaussian line and add a PEXMON model (Nandra et al. 2007) which self–consistently describes the reflection continuum and most important emission lines arising

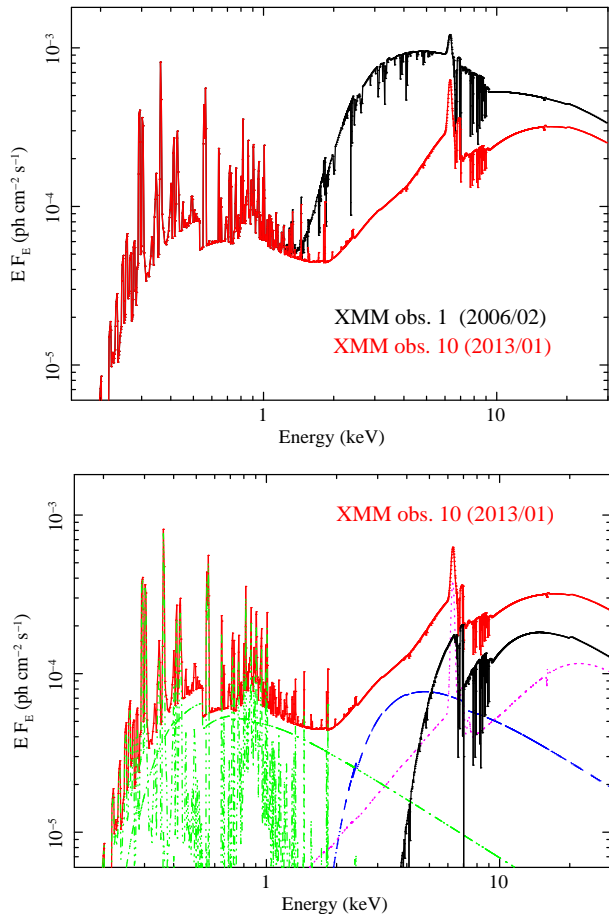


Figure 3. The best-fitting models for *XMM-Newton* observations 1 and 10 are shown in the upper panel and are extrapolated to higher energies than the data (i.e. to energies ≥ 10 keV) for clarity. In the lower panel, we replot the total best-fitting model for the more absorbed *XMM-Newton* observation 10, but include also all spectral components. The soft X-ray band below ~ 2 keV is described by extended (constant) emission comprising a power law contribution and optically-thin emission from collisionally-ionized plasma (dot-dashed lines, green in the on-line version). The hard X-ray band comprises contributions from (i) an heavily absorbed power law representing the intrinsic nuclear continuum (solid black line); (ii) an unabsorbed X-ray reflection component from optically-thick matter (dotted line, magenta in the on-line version); (iii) and additional power law contributing mainly in the 2–4 keV band and absorbed by a lower column density than the intrinsic nuclear continuum (dashed line, blue in the on-line version).

from an illuminated slab of optically-thick gas¹. As our spectral fits suggest that the Fe emission line has constant intensity with $I_{\text{Fe,obs. 1}} = (1.6 \pm 0.4) \times 10^{-5}$ ph cm⁻² s⁻¹ and $I_{\text{Fe,obs. 10}} = (1.8 \pm 0.2) \times 10^{-5}$ ph cm⁻² s⁻¹, we force all PEXMON parameters to be the same at both epochs. We convolve the reflection model with a Gaussian kernel to allow for some non-zero width

¹ The PEXMON model links the reflection continuum to the Fe line intensity assuming a disc-like geometry. As shown e.g. by Murphy & Yaqoob 2009, this is not always appropriate for a torus-like geometry. However, using two separate models for the Fe emission line and the reflection continuum gives exactly the same results as the PEXMON model, with the sum of the Fe line and reflection continuum models being coincident with the overall PEXMON model we use. In summary, there are no strong indications in the data against the use of the PEXMON model.

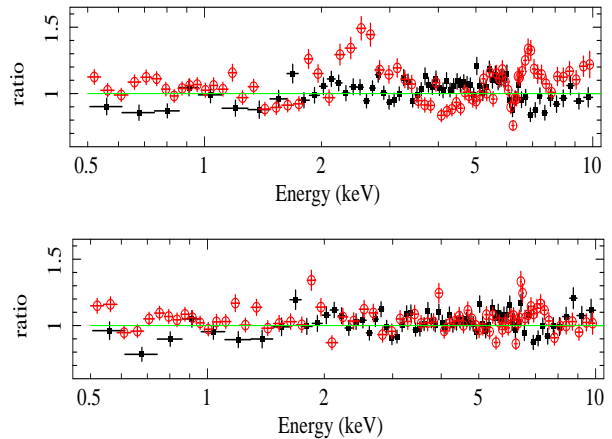


Figure 4. In the upper panel we show the data-to-model ratio for observations 1 and 10 before including the additional absorbed power law component ($\chi^2 = 1750$ for 1442 dof). In the lower panel, we show the final, best-fitting data-to-model ratio for both observations ($\chi^2 = 1499$ for 1439 dof).

of the emission lines. The illuminating spectral index is set to be the same as that of the intrinsic continuum, we assume Solar abundances and an inclination of 45° , so that the only free parameter of the reflection model is its normalisation (which is the same at both epochs). As we assume constant reflection, the reflection fraction R varies with the source intrinsic flux. As an example, we here report its value ($R \sim 0.65$) for observation 1 only. The statistical description of the data improves to $\chi^2 = 1750$ for 1442 dof (to be compared with $\chi^2 = 1875$ for 1440 dof when the simpler Gaussian emission-line model was used). However, as for all the models used above, the 2–4 keV residuals of observation 10 shown in Fig. 2 are not accounted for.

After a series of further tests², we find that the data can be described at both epochs with the addition of a further power law absorbed by a column density different than that of the primary one, whose physical nature is discussed in Section 3.3. The normalisation of this component is allowed to vary between the two epochs. The statistical description of the data is now excellent with a $\chi^2 = 1495$ for 1438 dof. As the additional power law is absorbed by two column densities that are consistent with each other in the two observations (and of the order of $7 - 8 \times 10^{22}$ cm⁻²), we force the column density to be the same at both epochs which results into $\chi^2 = 1499$ for 1439 dof. The best-fitting models for both observations are shown in the upper panel of Fig. 3. In the lower panel, we show the total best-fitting model for the more absorbed *XMM-Newton* observation 10, together with all spectral components. In Fig. 4, we compare the residuals obtained without (upper panel) and with (lower panel) the inclusion of the additional absorbed power law component. Some residuals are present around 6–7 keV, a possible signature of an extra-component or of some inadequacy of the ZXIPCF absorber model. However, we refrain from modelling these residuals by adding further ad-hoc absorption/emission lines to an already complex model. The overall reduced χ^2 is already 1.04 so that adding more complexity to the

² Replacing the neutral PEXMON reflection model with a ionized one (the REFLION model by Ross & Fabian 2005) and/or allowing for a partial covering solution for the neutral absorber does not reproduce the data well.

spectral model would imply the risk of over-modelling the data (see, however, Section 5.3 for a further discussion).

Having found a good description of the X-ray spectrum of ESO 323–G77, we can now critically consider some of the assumptions we made. We first allow the intrinsic spectral index to be different. However, the two spectral indices are consistent with each other with $\Gamma_{\text{obs. 1}} = 1.98 \pm 0.08$ and $\Gamma_{\text{obs. 10}} = 1.96 \pm 0.07$. We then consider possible variations in the warm absorber parameters. We keep the outflow velocities linked between the two epochs, and we first allow for variations in the ionization parameter only, but no improvement is obtained. The same holds for variations in the warm absorbers column density. We must point out, however, that the warm absorbers have little effect on the more absorbed observation 10, so that their properties are in fact mostly set by the less absorbed observation 1. Hence, we conclude that the only significant difference between the two spectra is a one order of magnitude variation in the column density towards the nuclear continuum (with $N_{\text{H}}^{\text{nuc1}} \simeq 5 - 6 \times 10^{22} \text{ cm}^{-2}$ during the *XMM-Newton* observation 1 and $N_{\text{H}}^{\text{nuc1}} \simeq 6 \times 10^{23} \text{ cm}^{-2}$ during observation 10). The best-fitting parameters will be reported later on, when the multi-epoch spectral results are presented (Section 4).

3.2 Short-timescale variability

As clear from the lower panel of Fig. 3, our spectral model predicts no short-timescale variability below ~ 2 keV as all soft components are expected to originate in distant material. On the other hand, the intrinsic, absorbed, nuclear continuum dominates in the 4–10 keV band so that some variability may be in principle expected. As for the additional absorbed power law, this component dominates in the intermediate 2–4 keV band. The *XMM-Newton* observation 10 is long enough (~ 120 ks) to investigate the short-timescale variability in different energy bands. We use light curves with 5000 s bins to compute the rms variability amplitude in the following energy bands: 0.5–1 keV, 1–2 keV, 2–4 keV, 4–6 keV, and 8–11 keV. We avoid the 6–8 keV band because this spectral range is not dominated by one single component, bearing contributions from continuum, reflection, and from the additional power law. All rms variability amplitudes are consistent with zero, except that in the 4–6 keV and 8–11 keV bands that are dominated by the absorbed intrinsic continuum. For those bands, we measure a rms variability amplitude of $\sim 0.11 \pm 0.04$. Therefore, the variability properties provide support to our spectral model, indicating that short-timescale variability is only present in energy bands that are dominated by the nuclear continuum. Moreover, the energy-dependent variability also shows that the additional absorbed power law dominating the 2–4 keV band (see Fig. 3, lower panel) is less variable than the intrinsic continuum. This is shown in the top panel of Fig. 5, where the light curves in the continuum-dominated 4–6 keV and 8–11 keV energy bands (upper and lower curves) are compared with that in the 2–4 keV band (middle curve), which is dominated by the additional absorbed power law component.

The observed short-timescale variability in the continuum-dominated bands can also be used to investigate whether intra-observation X-ray absorption variability is present. As seen in the lower panel of Fig. 3, the 8–11 keV band is (almost) insensitive to column density variations, while the softer 4–6 keV band is instead sensitive to variations of $N_{\text{H}}^{\text{nuc1}}$. Hence, the ratio between the two energy bands can highlight any intra-observation spectral variability due to absorption changes. The ratio of the 8–11 keV to the 4–6 keV band light curves is shown in the lower panel of Fig. 5. No spectral variability is detected, and the ratio is consistent with being

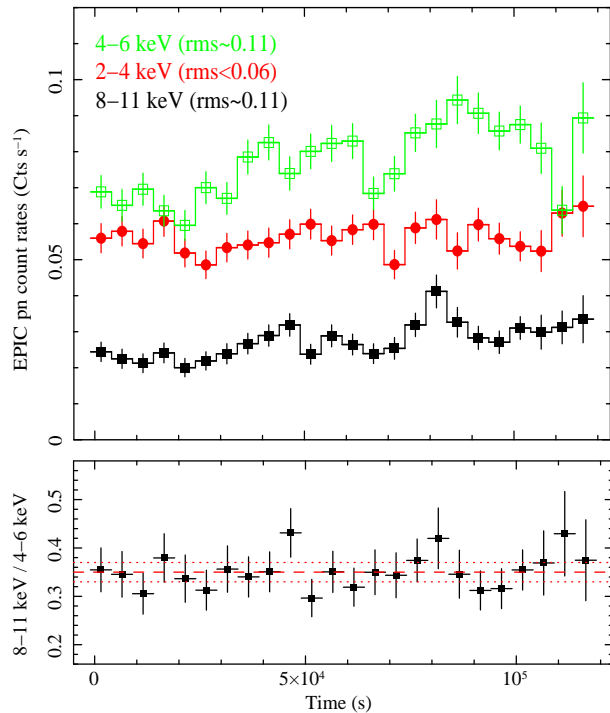


Figure 5. In the upper panel, we show the *XMM-Newton* observation 10 EPIC pn light curves in the 4–6 keV (upper curve), 2–4 keV (middle), and 8–11 keV (lower) energy bands. The bin size is 5000 s. In the lower panel of the figure, we show the ratio between the two continuum-dominated energy bands of 8–1 keV and 4–6 keV together with the best-fitting constant and its 90 per cent uncertainties (0.35 ± 0.02).

constant throughout the observation (a fit with a constant produces $\chi^2 = 16$ for 23 dof). We then conclude that no intra-observation absorption variability is detected during the 120 ks exposure of observation 10.

3.3 Physical interpretation for the additional absorbed power law component

The best-fitting spectral components shown in the lower panel of Fig. 3 are all typical of the X-ray spectra of AGN except the additional absorbed power law component that we introduced to account for the 2–4 keV residuals during the more absorbed *XMM-Newton* observation 10 (see e.g. Fig. 3 and Fig. 4). Hence, the inclusion of such additional component deserves some more detailed physical explanation. We interpret this component as scattering of the nuclear continuum in a clumpy absorber. Indeed, if the absorber is clumpy, the observed continuum comprises a transmitted component, namely an absorbed power law with column density set by that of the particular clump (or clumps) that happens to be on our line of sight (LOS), plus a scattering component due to clumps out of the LOS that intercept and scatter the nuclear continuum, re-directing part of it into our LOS. As this component likely arises from a number of different clumps, the scattered component is absorbed by the average column density of the clumpy absorber rather than that of one particular clump, which explains why the column density towards the transmitted and scattered components may be different and why the column density towards the scattered component is consistent with being always the same (see e.g. Yaqoob 2012 for a detailed discussion of the envisaged geometry, in partic-

ular his Fig. 2 and Section 7). Modelling the scattered component with a simple absorbed power law is only a zeroth-order approximation of the likely spectral shape which encodes our ignorance of the true scattering geometry. Notice that our scattering interpretation is consistent with the lower variability amplitude (if any is present) of the 2–4 keV band with respect to energy bands that are dominated by the continuum, as scattering in a relatively extended medium tends to wash out any intrinsic variability.

If our interpretation is correct, the scattering component is likely to be a fixed fraction of the intrinsic continuum, representing the scattering efficiency for a given geometry and physical condition of the scattering medium. To test this further hypothesis we modify our best-fitting model for the *XMM-Newton* observations 1 and 10 forcing the scattered continuum to be a constant fraction of the intrinsic nuclear continuum in both observations. We indeed find that the scattered component is consistent with a constant fraction ($14 \pm 3\%$) of the nuclear continuum, with a final statistic of $\chi^2 = 1500$ for 1440 dof, to be compared with $\chi^2 = 1499$ for 1439 dof when the scattered component is free to vary independently. As the two fits are statistically equivalent, we retain this further assumption in subsequent analysis. In summary, our interpretation suggests the presence of a variable, clumpy absorber whose properties can be investigated in great detail thanks to the remarkable absorption variability of ESO 323–G77 (see Fig. 1). The remaining part of this paper is devoted precisely to this goal.

3.4 The Compton-thick nature of the Suzaku observation

Before proceeding with a multi-epoch spectral analysis of all available X-ray observations, we point out that the *Suzaku* observation 9 on 2011/07 deserves some dedicated study. As clear from Fig. 1 (upper panel), the *Suzaku* observation is reflection-dominated with a very prominent Fe $K\alpha$ emission line whose equivalent width is ~ 800 eV. However, the XIS data (up to 10 keV) cannot discriminate between two different scenarios that can give rise to reflection-dominated spectra, namely a Compton-thick state where the nuclear continuum is heavily absorbed only marginally contributing below 10 keV, or a switched-off state where the nuclear continuum is extremely dim, only leaving the reprocessed components below 10 keV.

In principle, *Suzaku* is the ideal observatory to accurately measure the column density towards absorbed AGN thanks to the presence of the HXD and, in particular, the PIN detector with good sensitivity up to tens of keV. However, the large ($34' \times 34'$) field-of-view (FOV) of the HXD implies that the PIN X-ray data are contaminated by the nearby and relatively X-ray bright AGN ESO 323–G81, which is only $\sim 8.8'$ away from ESO 323–G77. No other relatively bright X-ray source is known within the HXD FOV. As such, we extract the spectra of both ESO 323–G77 and ESO 323–G81 from the XIS0 detector³ using circular regions of same radius (limited to $65''$ due to the position of ESO 323–G81, close to the XIS0 detector edge). We then build an overall spectral model for both ESO 323–G77 (for which we use the same model described in the previous section) and for ESO 323–G81 which is well described by a rather typical Seyfert 1 X-ray model comprising Galactic absorption, a power law continuum, a distant reflection

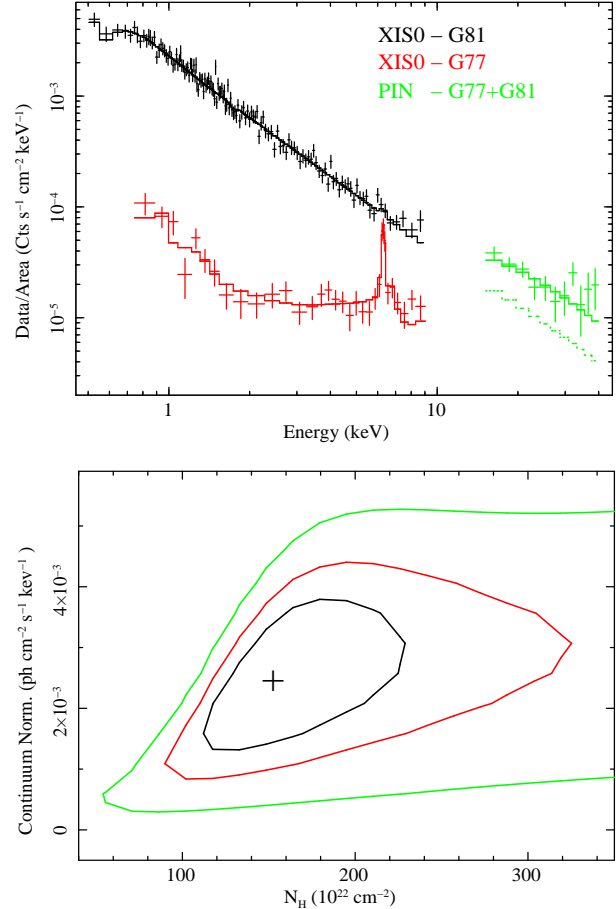


Figure 6. In the top panel we show the XIS0 spectra of ESO 323–G81 and ESO 323–G77 together with their best-fitting models (A and B respectively). The PIN spectrum comprises contribution from both sources. The best-fitting green solid line is for the A+B model, while the dotted line is the extrapolation of the best-fitting model B for ESO 323–G81. In the bottom panel, we show the 68, 90, and 99 per cent confidence level contours for intrinsic continuum column density and normalisation in ESO 323–G77, strongly suggesting a Compton-thick state for the *Suzaku* observation 9 of ESO 323–G77.

component, and a soft excess that we model here phenomenologically with a simple blackbody. Hereafter, the spectral models for ESO 323–G77 and ESO 323–G81 are called model A and B respectively.

We then fit the XIS 0 spectra of both sources simultaneously with the PIN spectrum, which comprises contributions from both. The XIS0 spectrum of ESO 323–G77 is described with model A, the XIS0 spectrum of ESO 323–G81 with model B, and the PIN spectrum with model A+B. We fix the PIN/XIS0 cross-calibration constant to the value of 1.16 for ESO 323–G77, which is appropriate for observations performed at the XIS nominal position. The position of ESO 323–G81 (close to the west edge of the XIS detectors) falls closer to the HXD nominal position⁴. Hence we use a cross-calibration constant of 1.18 (the value appropriate for the HXD nominal position) for ESO 323–G81. However, we must point out that our results are basically insensitive to this conservative choice.

In the top panel of Fig. 6 we show the XIS0 spectra of

³ The reason for using only the XIS0 data (and not the XIS3 as well) in this analysis is to not introduce further cross-calibration uncertainties between the XIS and PIN detectors.

⁴ Maeda et al. 2008, JX-ISAS-SUZAKU-MEMO-2008-06

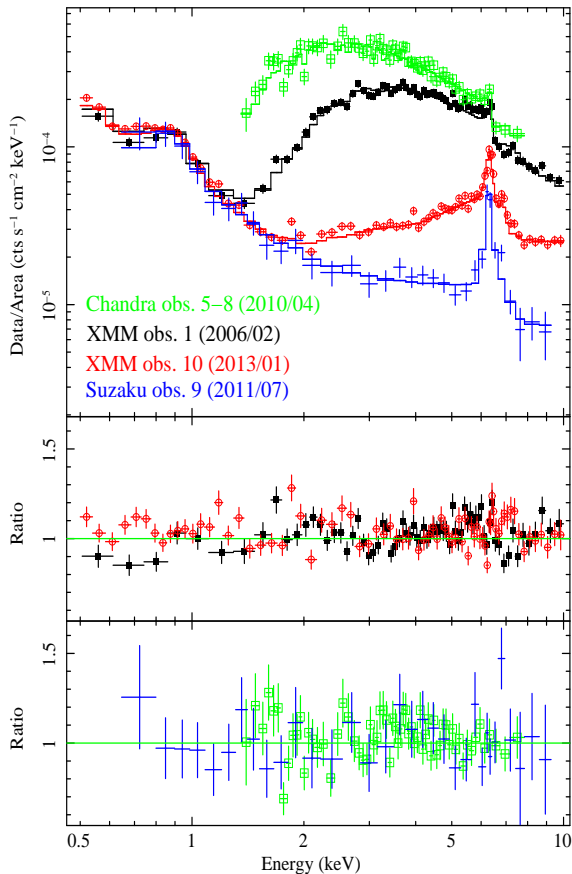


Figure 7. Data (divided by the corresponding detector effective area), best-fitting model, and data-to-model ratio for the final multi-epoch spectral analysis. We only show the highest quality observations from *XMM-Newton* (observations 1 and 10), *Chandra* (observation 5–8; only the HEG data are shown), and *Suzaku* (observation 9) for clarity. The middle panel shows the best-fitting data-to-model ratio for the two *XMM-Newton* observations 1 and 10, while the lower panel is for the *Chandra* and *Suzaku* observations 5–8 and 9.

ESO 323–G77 and ESO 323–G81, together with the PIN spectrum and the corresponding best-fitting model(s). The dotted line represents the extrapolation of model B (the best-fitting model for ESO 323–G81) in the PIN band and highlights the hard X-ray excess that we attribute to ESO 323–G77. The extrapolation of model B to the PIN band suggests that ESO 323–G81 has a 15–40 keV flux of $(9.0 \pm 1.0) \times 10^{-12} \text{ erg s}^{-1} \text{ cm}^{-2}$. On the other hand, the observed PIN flux is $(1.99 \pm 0.23) \times 10^{-11} \text{ erg s}^{-1} \text{ cm}^{-2}$ in the same band, i.e. more than a factor of 2 higher. In the bottom panel Fig. 6 we show the 68, 90, and 99 per cent confidence level contours for the absorber column density towards the intrinsic nuclear continuum in ESO 323–G77 and for the continuum normalisation. Although the systematic errors due to the extrapolation of model B in the PIN band may affect the uncertainties, our analysis strongly suggests a nearly Compton-thick or Compton-thick state for the 2011/07 *Suzaku* observation of ESO 323–G77 with $N_{\text{H}} \geq 9 \times 10^{23} \text{ cm}^{-2}$ at the 90 per cent confidence level for any allowed intrinsic flux level.

4 MULTI-EPOCH SPECTRAL ANALYSIS

We now apply the spectral model discussed above to the multi-epoch data, i.e. to all spectra shown in the upper and lower panels of Fig. 1. As the *Swift* XRT data only have a minimum of 5 counts per energy bin, we apply the C-statistic for these data, and the standard χ^2 minimisation for all the others. We also use the 90 per cent confidence levels results discussed for the column density during the *Suzaku* observation to impose that $N_{\text{H}}^{\text{Suzaku}} = (1.5_{-0.6}^{+1.7}) \times 10^{24} \text{ cm}^{-2}$ (see Fig. 6, lower panel).

All data are fitted simultaneously in the 0.5–10 keV band (or in restricted detector-dependent energy bands, depending on the data quality). In the same way as for the analysis of the two *XMM-Newton* observations discussed above, most parameters are allowed to vary during the fit, but are forced to be the same at all epochs. In particular, we force constant spectral index, soft X-ray components temperatures and normalisations, reflection flux, and warm absorbers properties at all epochs. The column density towards the additional absorbed power law is also forced to be the same at all epochs, under the assumption that it represents the average clumpy absorber column density along many different LOS. Moreover, the (hard) scattered component is assumed to be a constant fraction of the nuclear continuum, i.e. we force the same scattered fraction at all epochs. The free parameters that are instead allowed to vary independently are only the column density towards the intrinsic continuum, and the continuum normalisation.

We reach an overall excellent description of the data with $\chi^2 = 2616$ for 2597 dof, and $C = 137$ for 117 dof. The spectra, best-fitting models, and data to model ratios for the higher quality observations from *XMM-Newton* (obs. 1 and 10), *Chandra* (obs. 5–8), and *Suzaku* (obs. 9) are shown in Fig. 7, while the best-fitting parameters are reported in Table 2. The most important result of our analysis is the detection of clear, unambiguous X-ray absorption variability due to changes of the column density of a neutral absorber towards the intrinsic nuclear continuum. Table 2 is separated into constant components (the soft power law and collisionally-ionized plasmas, the reflection component, and the warm absorbers) and variable or continuum-related components. We start our discussion with the former, while the latter will be discussed in Section 6.

5 RESULTS FROM THE SPECTRAL ANALYSIS

Multi-epoch X-ray observations of ESO 323–G77 from February 2006 to January 2013 reveal remarkable spectral variability associated with X-ray absorption variability. However, the overall spectral model is complex, and we discuss here the properties of all constant spectral components, deferring the discussion and interpretation of the variable absorber to Section 6.

5.1 X-ray reflection and soft X-ray emission

An X-ray reflection component comprising a narrow Fe $K\alpha$ line is detected at all epochs. All data are consistent with a constant reflection (and Fe $K\alpha$ emission line) flux, so that the observed Fe $K\alpha$ line equivalent width varies from $\sim 55 \text{ eV}$ during the highest flux *Chandra* observations 5–8 on 2010/04 to $\sim 800 \text{ eV}$ during the lowest flux *Suzaku* observation 9 on 2011/07. According to our spectral model, the X-ray reflection component is unabsorbed which, together with the constant reflection flux, suggests reflection from an extended medium with physical size similar or larger

Table 2. Best-fitting parameters from our multi-epoch spectral analysis. The final fitting statistic is excellent with $\chi^2/\text{dof} = 2616/2597$ for the higher quality data from *XMM-Newton* (obs. 1 and 10), *Chandra* (obs. 5–8), and *Suzaku* (obs. 9), and with $C/\text{dof} = 137/117$ for the lower quality *Swift* data (obs. 2, 3, and 4).

Constant components							
Continuum	Soft PL	APEC (1)		APEC (2)		Reflection	
Γ	$L_{0.5-2}^{\text{Soft PL}}$	$kT^{(1)}$	$L_{0.5-2}^{(1)}$	$kT^{(2)}$	$L_{0.5-2}^{(2)}$	L_{2-10}^{ref}	σ^{ref}
1.98 ± 0.06	$(6.7 \pm 0.3) \times 10^{-2}$	0.74 ± 0.05	$(2.7 \pm 0.2) \times 10^{-2}$	0.09 ± 0.02	$(9 \pm 1) \times 10^{-3}$	0.31 ± 0.02	≤ 0.06
		Warm absorber (1)		Warm absorber (2)			
		$N_{\text{H}}^{(1)}$	$\log \xi^{(1)}$	$v_{\text{out}}^{(1)}$	$N_{\text{H}}^{(2)}$	$\log \xi^{(2)}$	$v_{\text{out}}^{(2)}$
		9 ± 6	3.4 ± 0.3	3500 ± 700	35 ± 18	4.1 ± 0.3	1500 ± 600
Variable/continuum components							
Obs. #	Intrinsic nuclear continuum			Scattered continuum		Total	
	$N_{\text{H}}^{\text{nucl}}$	F_{2-10}^{nucl}	L_{2-10}^{nucl}	$N_{\text{H}}^{\text{scatt}}$	$L^{\text{scatt}}/L^{\text{nucl}}$	$F_{0.5-2}^{\text{tot}}$	F_{2-10}^{tot}
1	5.6 ± 0.4	7.3 ± 0.1	6.7 ± 0.4	7.6 ± 0.8	0.15 ± 0.03	0.24 ± 0.01	9.2 ± 0.1
2	50 ± 18	7 ± 4	5 ± 3	"	"	0.19 ± 0.06	3.5 ± 0.8
3	5.4 ± 0.9	7 ± 2	6 ± 2	"	"	0.24 ± 0.05	8.3 ± 0.7
4	5 ± 1	8 ± 2	7 ± 2	"	"	0.28 ± 0.06	10 ± 1
5-8	2.7 ± 0.3	11.0 ± 0.3	8.4 ± 0.5	"	"	0.63 ± 0.01	13.2 ± 0.3
9	150_{-60p}^{+150}	0.4 ± 0.2	3 ± 2	"	"	0.16 ± 0.01	0.9 ± 0.1
10	60 ± 7	1.05 ± 0.06	4.5 ± 0.5	"	"	0.17 ± 0.01	2.6 ± 0.1

Units: luminosities are unabsorbed and given in units of $10^{42} \text{ erg s}^{-1}$; fluxes are as observed and given in units of $10^{-12} \text{ erg cm}^{-2} \text{ s}^{-1}$; the temperature of the APEC components is given in keV and the same units are also used for the width σ^{ref} of the Gaussian kernel that is applied to the reflection model (the upper limit on the kernel width corresponds to $\leq 6600 \text{ km s}^{-1}$ in FWHM, consistent with any Fe line production site from the broad-line-region outwards). Column densities are given in units of 10^{22} cm^{-2} , and the warm absorbers outflow velocities are in units of km s^{-1} . The subscript p for the value of $N_{\text{H}}^{\text{nucl}}$ of observation 9 means that the parameter pegged to its minimum allowed value (see Section 3.4).

than that of the X-ray absorber(s). We measure a 2–10 keV reflected luminosity of $L_{2-10}^{\text{ref}} \sim 3.1 \times 10^{41} \text{ erg s}^{-1}$, i.e. about 5 % of the averaged 2–10 keV nuclear luminosity of ESO 323–G77 ($\sim 5.8 \times 10^{42} \text{ erg s}^{-1}$).

The soft X-ray band is here modelled with two constant components, namely a power-law and collisionally-ionized plasma emission. The soft X-ray model has to be considered as the simplest phenomenological description of the data. However, the two constant components can be identified with (i) scattering of the nuclear continuum in an extended medium (possibly the narrow line region, see Bianchi, Guainazzi & Chiaberge 2006), and (ii) the contribution of star-forming regions or shocked gas in the AGN environment and host galaxy. The soft 0.5–2 keV luminosity associated with the power law is $L_{0.5-2}^{\text{PL}} \sim 6.7 \times 10^{40} \text{ erg s}^{-1}$, while the two plasma emission models contribute a total luminosity of $L_{0.5-2}^{\text{APEC}} \sim 3.6 \times 10^{40} \text{ erg s}^{-1}$.

$L_{0.5-2}^{\text{PL}}$ represents about 1–2 % of the averaged intrinsic nuclear luminosity extrapolated to the same band, to be compared with a 1–5 % typical soft X-rays scattered fraction in obscured AGN (e.g. Bianchi & Guainazzi 2006).

On the other hand, the soft X-ray luminosity associated with the thermal plasma emission components can be used to estimate the star-formation-rate (SFR) in the galaxy, under the (strong) assumption that the observed luminosity is due to star-formation. In fact, as seen in the soft X-ray spectra of many obscured AGN, part of the emission-line spectrum in the soft X-ray band is often due to emission from gas that is photo-ionized by the AGN rather than collisionally-ionized in shocks and/or star-forming regions

(Guainazzi & Bianchi 2007). Hence, by assuming that the luminosity of our APEC models is entirely associated with star-formation, we can only derive an upper limit on the SFR in ESO 323–G77. By using the relationship $\text{SFR}_{\text{X}} \simeq 2.2 \times 10^{-40} L_{0.5-2} M_{\odot} \text{ yr}^{-1}$ (Ranalli, Comastri & Setti 2003), the X-ray-based estimate of the SFR in ESO 323–G77 is $\text{SFR}_{\text{X}} \simeq 6 \pm 3 M_{\odot} \text{ yr}^{-1}$, and thus $\text{SFR}_{\text{X}} \lesssim 9 M_{\odot} \text{ yr}^{-1}$.

Esquej et al. (2013) derive the SFR in ESO 323–G77 on different scales, using the 11.3 m polycyclic aromatic hydrocarbon (PAH) feature as a proxy of the SFR. Using high angular-resolution MIR spectroscopic observations at the VLT/VISIR (originally presented by Hönig et al. 2010), they obtain an upper limit on the nuclear SFR of $\text{SFR}_{\text{nuc}} \lesssim 0.23 M_{\odot} \text{ yr}^{-1}$ within the inner $\sim 200 \text{ pc}$. On the other hand, lower angular-resolution *Spitzer* data were used to estimate an extended SFR of $\text{SFR}_{\text{ext}} \simeq 3 M_{\odot} \text{ yr}^{-1}$ within $\sim 1 \text{ kpc}$ which is fully consistent with our $\text{SFR}_{\text{X}} \lesssim 9 M_{\odot} \text{ yr}^{-1}$. We point out that the X-ray data are typically extracted from circular regions of 20 – 40 '' radius which correspond to an encircled radius of $\sim 6 - 12 \text{ kpc}$ at the distance of ESO 323–G77.

5.2 The highly-ionized absorbers

We confirm the detection of two highly-ionized, outflowing warm absorbers in ESO 323–G77, as firstly reported by Jiménez-Bailón et al. (2008a) in their analysis of the *XMM-Newton* observation 1. Although we assume, for simplicity and because the data allow us to do so, that the parameters of the warm absorbers are the same at all epochs, it is clear the the absorbers have little, if any, effect

on significantly absorbed observations, and they can only be constrained reliably from the least absorbed and high quality *XMM–Newton* observation 1 and *Chandra* observation 5–8. We then repeat the analysis by only considering these data sets, in the attempt of investigating the warm absorbers parameters in some more detail. In this analysis, we allow the ionization state of the two absorbers to vary between the different epochs, while keeping outflow velocities and column densities tied in all data sets.

The outflow velocities and column densities turn out to be consistent with those reported in Table 2. As for the ionization parameters, only marginal variability is observed, with an overall $\Delta\chi^2 = 5$ for 2 additional free parameters. On the other hand, both the observed flux and the intrinsic nuclear luminosity during the two observations are within a factor of 2 from each other, and the uncertainties in the warm absorbers ionization parameters do not allow us to study their response to the continuum variation at such a fine level (see Table 2).

Let us consider here the possible origin of such highly-ionized outflow. One possibility is that the outflow is part of a disc-wind launched off the inner accretion flow, where radiation pressure is sufficient to accelerate gas up to escape velocities. As discussed in Section 6, typical launching radii are of the order of few hundreds of r_g (e.g. Risaliti & Elvis 2010), where the escape velocity is of the order of $1 - 3 \times 10^4 \text{ km s}^{-1}$, i.e. about one order of magnitude higher than the observed outflow velocity of $1 - 4 \times 10^3 \text{ km s}^{-1}$. Hence, the wind has to be accelerated along a direction that is almost perpendicular to our LOS to be consistent with the relatively low outflow velocity we measure. This is unlikely, to say the least, given that our LOS has a most probable inclination of $\sim 45^\circ$ with respect to the symmetry axis (Schmid et al. 2003; Smith et al. 2004). Assuming a given misalignment between the outflow direction and our LOS, one can infer limits on the outflow launching radius R_{wind} by assuming that the observed outflow velocity corresponds to the component along the LOS of the escape velocity at the launching radius. For $v_{\text{out}} = 1 - 4 \times 10^3 \text{ km s}^{-1}$ and a LOS-outflow misalignment of $0^\circ - 25^\circ$, $R_{\text{wind}} = 0.1 - 2.7 \times 10^5 r_g = 0.4 - 9.6 \times 10^{17} \text{ cm}$ which suggests a physical scale of the order of (or even slightly larger than) that of the BLR rather than of the inner disc ($R_{\text{BLR}} \sim 1 - 2 \times 10^{16} \text{ cm}$ according to Kaspi et al. 2005 for the mean 2–10 keV luminosity of ESO 323–G77, i.e. $\sim 5.8 \times 10^{42} \text{ erg s}^{-1}$). It is therefore tempting to associate the ionized gas with a warm/hot medium that may fill the intra-cloud BLR, possibly enabling the cold, line-emitting clumps of the BLR to be pressure-confined.

5.3 A relativistic, broad Fe K α line?

In their analysis of the *XMM–Newton* observation 1 on 2006/02, Jiménez-Bailón et al. (2008a) report the detection of a relativistically broadened Fe K α emission line. Their best-fitting model comprises a broad 6.4 keV line off the inner accretion disc of a spinning Kerr black hole viewed at $\sim 26^\circ$ inclination. Adding a LAOR line model with rest-frame energy fixed at 6.4 keV to our best-fitting solution for the same observation, the fitting statistic improves significantly with $\Delta\chi^2 = 17$ for 4 additional free parameters, and most of the residuals shown in the lower panel of Fig. 4 around 6–7 keV are accounted for. We confirm their main findings, and we measure a line equivalent width of $280 \pm 180 \text{ eV}$ with respect to the intrinsic nuclear continuum, a disc inclination of $26^\circ \pm 7^\circ$ and a disc inner radius of $\leq 10 r_g$, for which any black hole spin is allowed. We measure a rather typical radial emissivity index of 2.5 ± 0.5 . We point out that the remaining parameters of

the global model are all consistent with the results of Table 2 within the quoted uncertainties.

We then apply the same model to the multi-epoch data forcing, for simplicity, all line parameters except the normalisation to be the same in all data sets with sufficiently high quality, namely the *XMM–Newton* observations 1 and 10, and the *Chandra* observations 5–8. We do not consider the good quality *Suzaku* data here, because the Compton-thick absorption towards the X-ray source prevents the detection of any contribution from the innermost accretion flow. The fitting statistic before applying the broad line model is $\chi^2 = 2410$ for 2435 dof, and the improvement obtained with the addition of the broad line is $\Delta\chi^2 = 22$ for 6 additional free parameters. However, the line is not formally detected during the 2010/04 *Chandra* observation 5–8, and is only marginally detected during the 2013/01 *XMM–Newton* observation 10. All broad line parameters are consistent with those derived for the *XMM–Newton* observation 1. The resulting line equivalent widths are $280 \pm 180 \text{ eV}$, $\leq 108 \text{ eV}$, and $60 \pm 50 \text{ eV}$ for the *XMM–Newton* observation 1, *Chandra* observation 5–8, and *XMM–Newton* observation 10, respectively. Hence the data are marginally consistent with a constant line equivalent width of $\sim 100 \text{ eV}$, which would indicate that the line responds to the intrinsic continuum variation. We must, however, point out that while a broad feature that is consistent with a relativistic Fe line is indeed detected in the *XMM–Newton* observations 1 and 10 and is allowed in the *Chandra* observation 5–8, the complexity of our spectral model prevents us to claim the secure detection of a broad relativistic line in ESO 323–G77, as other interpretation of this spectral feature may be possible (e.g. Turner & Miller 2009).

5.4 The scattered component

As already discussed in Section 3.3 we interpret the additional absorbed power law that we need to account for the spectral shape of the *XMM–Newton* observation 10 as a scattering component originating in a clumpy absorber. Our analysis of the X-ray absorption variability in ESO 323–G77 confirms the presence of such clumpy absorber and therefore supports our interpretation (see also the Section 6). Notice that a similar scattered component was suggested also in NGC 7582 (Piconcelli et al. 2007) and NGC 3277 (Lamer, Uttley, McHardy 2003), two sources where X-ray absorption variability is also present suggesting the presence of a clumpy absorber (most likely the BLR).

As mentioned, the amount of optical polarisation as well as the orientation of the position angle with respect to the [O III] ionization cone, strongly suggests that we are seeing the nucleus with $\sim 45^\circ$ inclination. Assuming that the half-opening angle of the clumpy torus is similar, our LOS likely intercepts the torus atmosphere. A sketch of the envisaged nuclear geometry in ESO 323–G77 is shown in Fig. 8. In such situation, scattering can arise in the clumpy torus itself, from LOS with higher inclination than ours, so that the scattered component emission reasonably intercepts more clumps than the intrinsic nuclear continuum (e.g. the situation shown in Fig. 8). Indeed, we measure a column density of $N_{\text{H}}^{\text{scatt}} = 7 - 8 \times 10^{22} \text{ cm}^{-2}$ towards the scattered component, and a (variable) column density of $N_{\text{H}}^{\text{nuc1}} = 2 - 6 \times 10^{22} \text{ cm}^{-2}$ towards the nuclear continuum, possibly indicating that the scattered component goes through more absorbing clouds than the nuclear emission into our LOS. Notice that scattering can also arise from BLR clouds and not only from the clumpy torus itself.

The scattered component we propose in fact detectable only in cases where the intrinsic nuclear continuum is more absorbed

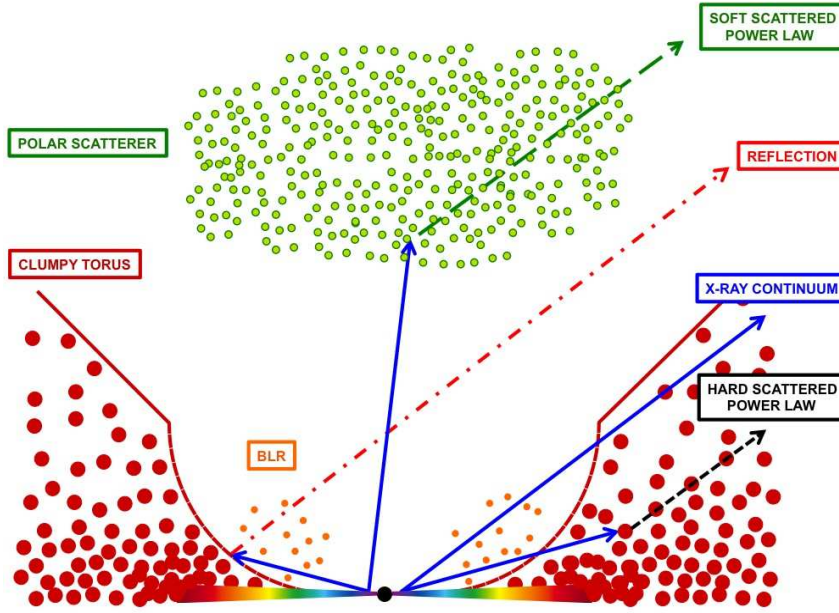


Figure 8. A sketch of a possible geometry for the systems of absorbers, as suggested by the X-ray data. We assume an inclination angle of $\sim 45^\circ$, and our LOS is on the right-hand-side of the figure. The intrinsic nuclear continuum is shown with solid lines (blue in the on-line version) and goes through one cloud of the clumpy torus. This situation is therefore appropriate for observations 1, 3, 4, and 5-8. The remaining observations correspond instead to one of the BLR clouds crossing our LOS. The continuum illuminates a polar scattering region which gives rise to the soft scattered power law component which is likely associated with part of the soft emission lines spectrum (long-dashed line, green in the on-line version). For simplicity, we do not show star-forming regions that may be associated with the plasma emission model. The continuum also illuminates the far side of the clumpy torus which, at least at low latitudes, is likely optically-thick, producing the X-ray reflection spectrum (dot-dashed line, red in the on-line version). Finally, the X-ray continuum intercepts clouds in the clumpy torus (and/or the BLR) out of our LOS. These clouds scatter part of the irradiating continuum into our LOS giving rise to a hard scattered power-law (short-dashed black line) that is absorbed by a different column density than the X-ray nuclear continuum, as it generally goes through a different system of clouds.

than the scattered component itself. Hence, we do not expect to detect this component in typical unabsorbed Seyfert 1 galaxy, although it may be ubiquitous in the X-ray spectra of AGN. On the other hand, we suggest that the scattered component should be detected in all Seyfert 1 galaxies whose nuclear continuum is transiently obscured by clouds with column density in excess of $\text{few} \times 10^{22} \text{ cm}^{-2}$. As for genuine Compton-thin and/or Compton-thick Seyfert 2 galaxies with highly inclined LOS, the scattered component should still be present, but significantly more absorbed than in ESO 323-G18 which may yield to its detection in some cases, but probably not in those where the nucleus is seen edge-on (or nearly edge-on) where the difference in column density between the nuclear continuum and the scattered component may be too small.

In principle, the scattered component is likely to contribute some line emission in the Fe K band which may be variable if scattering occurs off clouds that are close to our LOS. However, if the scattered flux is only $\sim 15\%$ of the intrinsic (see Table 2), the Fe line flux likely comprises $\lesssim 15\%$ contribution from the scattered component. Our data are consistent with a constant Fe line flux, but we cannot exclude the presence of a small variable component of the Fe emission line at such a fine level (as an example, the Fe line flux is only constrained at the $\sim 25\%$ level in the *XMM-Newton* observation 1.)

As for the reflection component, the Fe line width of 0.06 keV (corresponding to a $\text{FWHM} \leq 6600 \text{ km s}^{-1}$) is consistent with any possible physical scale from the inner BLR outwards. In Fig. 8 we

show only one possible origin for such component, i.e. the far side of the clumpy torus at low elevation, where the dusty gas is likely optically-thick. However, our analysis cannot rule out that reflection arises (or also arises) in material that is either closer (e.g. the BLR or the near side of the torus) or farther away (see e.g. Iwasawa et al 2003; Guainazzi et al. 2012) than the far side of the clumpy torus itself.

6 THE VARIABLE ABSORBER

Fig. 9 shows the column density towards the intrinsic nuclear continuum as a function of time, summarising the most important result of our multi-epoch spectral analysis, namely the remarkable X-ray absorption variability towards the nuclear continuum in ESO 323-G77. The 2006 observations (1 to 4 in Table 1) are shown in the left panel, and the remaining 2010–2013 ones in the right panel. The less X-ray absorbed state is observed during the *Chandra* monitoring from 2010-04–14 to 24 where the source appears to be seen through a column of $\sim 2.7 \times 10^{22} \text{ cm}^{-2}$. On the other hand, the *Suzaku* observation of 2011-07–20 is reflection-dominated and strongly suggests a Compton-thick state with a neutral absorber column density of $\sim 1.5 \times 10^{24} \text{ cm}^{-2}$. The other observations reveal intermediate-absorption states with neutral column densities ranging from $\sim 5 \times 10^{22} \text{ cm}^{-2}$ to $\sim 6 \times 10^{23} \text{ cm}^{-2}$.

The observed X-ray absorption variability allows us to study the properties of the absorbing systems in great detail. Let us as-

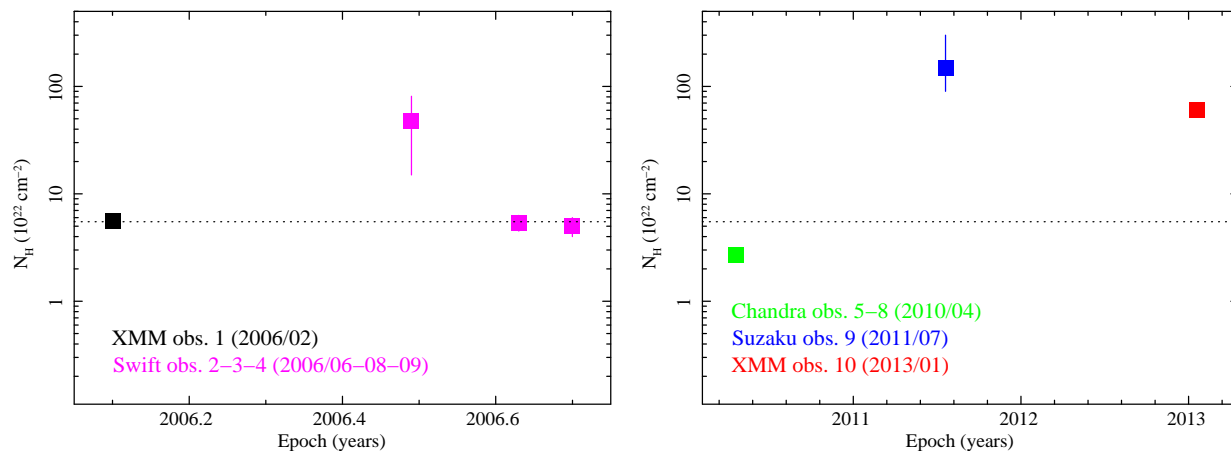


Figure 9. Column density of the variable neutral absorber as a function of observation epoch. The dotted line is the best-fitting column density to observations 1, 3, and 4 that appear to be absorbed by the same column of neutral gas.

sume the simplest possible geometry, namely an X-ray source with linear size D_s and an absorber (cloud) of uniform column density and size D_c (e.g. a sphere of diameter D_c). As our multi-epoch spectral analysis never reveals a partial covering structure, $D_c \geq D_s$. We also assume that the absorbing cloud moves with transverse velocity v_c with respect to our LOS. The most important timescale that can be derived from our analysis is ΔT_{const} , i.e. the timescale over which the X-ray source is covered by the same absorbing cloud. ΔT_{const} can be related to D_c , D_s , and v_c via $D_c = \Delta T_{\text{const}} v_c + D_s$, so that

$$\Delta T_{\text{const}}^{\text{min}} v_c^{\text{min}} + D_s \leq D_c \leq \Delta T_{\text{const}}^{\text{max}} v_c^{\text{max}} + D_s. \quad (1)$$

As for the X-ray source size, we impose $D_s \simeq 20 r_g$, in agreement with previous X-ray occultation results (e.g. NGC 1365, see Risaliti et al. 2007) and with micro-lensing results (e.g. Dai et al. 2010; Mosquera et al. 2013). For a black hole mass of $M_{\text{BH}} \simeq 2.5 \times 10^7 M_{\odot}$ (e.g. Wang & Zhang 2007), one has $D_s \simeq 7.4 \times 10^{13}$ cm.

Hereafter, we critically consider three possible origins for the variable absorber, namely (i) the classical torus of Unified models; (ii) the BLR; (iii) a disc-wind launched off the inner accretion disc. The three possible origins are spatially located at different scales and, under the reasonable assumption that the cloud transverse motion is dominated by gravity (except for the wind, where the wind outflow velocity plays a role), they are associated with different typical values for the cloud velocity.

The torus: the dusty torus inner boundary is identified with the dust sublimation radius $R_{\text{dust}} \simeq 0.4 L_{45}^{0.5}$ pc (Elitzur & Shlosman 2006), where L_{45} is the bolometric luminosity in units of 10^{45} erg s^{-1} . The averaged intrinsic luminosity of ESO 323–G77 is $\sim 5.8 \times 10^{42}$ erg s^{-1} in the 2–10 keV band. Assuming a 2–10 keV bolometric correction of 20, as appropriate for AGN with Eddington ratio ≤ 0.1 (e.g. Vasudevan & Fabian 2007), gives $L_{\text{Bol}} \sim 1.2 \times 10^{44}$ erg s^{-1} and $R_{\text{dust}} \simeq 0.14$ pc. As for the torus outer edge, current IR observations indicate that the outer edge of the torus is $R_{\text{out}} \simeq 5 - 30 R_{\text{dust}}$ (e.g. Nenkova, Ivezić & Elitzur 2002; Poncelet et al. 2006; Tristram et al. 2007; Nenkova et al. 2008b; Ramos Almeida 2011; Alonso-Herrero 2011). As we are interested in a conservative upper limit, we assume that $R_{\text{out}} = 5$ pc (corresponding to $\sim 35 \times R_{\text{dust}}$). Assuming Keplerian motion, one has $v_c^{\text{TOR}} = 150 - 900$ km s^{-1} .

The BLR: a natural upper limit on the BLR location is the

dust-sublimation radius itself. In fact, the BLR and torus are most likely part of the same obscuring structure which simply changes from gas- to dust-dominated at R_{dust} (e.g. Elitzur & Shlosman 2006), so that $v_c^{\text{BLR,min}} = 900$ km s^{-1} . As for the BLR inner maximum velocity, let us consider the observed broad H β line FWHM $\simeq 2500$ km s^{-1} (Winkler 1992), which is related to the actual cloud velocity by the BLR geometry and/or by our particular viewing angle. Assuming a spherical BLR, this translated into a cloud typical velocity $\simeq 2200$ km s^{-1} . For a disc-like, flattened BLR, the relationship between FWHM and actual velocity depends on the viewing angle, the velocity being higher for lower inclination angles of our LOS. As mentioned, there are important indications from spectro-polarimetry that our viewing angle is close to 45° in ESO 323–G77. In order to derive the most conservative cloud velocity upper limit, we assume here a lower inclination of 25° , which corresponds to $v_c^{\text{BLR,max}} = 3000$ km s^{-1} . Summarising, we have $v_c^{\text{BLR}} = 900 - 3000$ km s^{-1} .

The inner disc-wind: in recent years, the presence of a disc-wind launched off the inner accretion flow has been often invoked to account for spectral and variability properties of AGN in the X-ray band (e.g. Miller et al. 2010; Tombesi et al. 2010, 2012; Tatum et al. 2012). Theoretical modelling suggests that disc-winds are launched off radii of the order of $100 - 700 r_g$ on the accretion disc (Risaliti & Elvis 2010; Nomura 2013). The wind clumps transverse motion is likely dominated by gravity, although depending on the outflow direction with respect to the LOS, the outflow velocity may also play a significant role. Assuming that the latter equals the escape velocity at the launching radius, we can use the escape velocity at $100 r_g$ as an upper limit on the cloud velocity, and the Keplerian velocity at $700 r_g$ as a lower limit to infer that $v_c^{\text{WIND}} = 11000 - 42000$ km s^{-1} .

6.1 The few $\times 10^{22}$ cm $^{-2}$ absorber during observations 1, 3, 4, and 5-8

Let us first focus our attention on the observations absorbed by column densities of few $\times 10^{22}$ cm $^{-2}$, namely observations 1, 3, 4, and 5–8. As shown in Fig. 9, the 2006 observations 1, 3, and 4 appear to be absorbed by the same column density ($\sim 5.5 \times 10^{22}$ cm $^{-2}$), while a sudden increase of the column density [$\Delta N_{\text{H}} = (4.5 \pm 1.8) \times 10^{23}$ cm $^{-2}$] is observed during observation 2. It is tempting to regard the overall 2006 column density variability as due to a

constant-column-density absorber with $N_{\text{H}} \sim 5.5 \times 10^{22} \text{ cm}^{-2}$ covering the X-ray source during the 7 months spanned by observations 1 to 4 (2006/02 to 2006/09) plus an additional obscuration event taking place on 2006/06 during observation 2. On the other hand, the 2010/04 observation 5–8 (3.6 yr after observation 4) appears to be absorbed by a slightly lower column density of $N_{\text{H}} \sim 2.7 \times 10^{22} \text{ cm}^{-2}$.

The lack of absorption variability in 2006 (besides the event on 2006/06, observation 2) suggests that $\Delta T_{\text{const}} \geq 7$ months. On the other hand, no information of the upper limit on ΔT_{const} is available, due to the lack of data before 2006. Using Eq. 1 with the various v_c that we have derived in the previous Section and with $D_s = 7.4 \times 10^{13} \text{ cm}$, one has $D_c^{\text{TOR}} \geq 3.5 \times 10^{14} \text{ cm}$, $D_c^{\text{BLR}} \geq 1.7 \times 10^{15} \text{ cm}$, and $D_c^{\text{WIND}} \geq 2.0 \times 10^{16} \text{ cm}$. By combining the cloud size(s) with the maximum common column density during the 7 months corresponding to observations 1, 3, and 4 (namely $6 \times 10^{22} \text{ cm}^{-2}$), we obtain upper limits on the cloud number density for the three cases, i.e. $n_c^{\text{TOR}} \leq 1.7 \times 10^8 \text{ cm}^{-3}$, $n_c^{\text{BLR}} \leq 3.5 \times 10^7 \text{ cm}^{-3}$, and $n_c^{\text{WIND}} \leq 3.0 \times 10^6 \text{ cm}^{-3}$.

Only n_c^{TOR} is consistent with the density that is expected in the dusty torus (e.g. Elitzur & Shlosman 2006), while the upper limits on n_c^{BLR} and n_c^{WIND} are at least two orders of magnitude lower than the number density of the BLR and/or disc-wind. We conclude that the few $\times 10^{22} \text{ cm}^{-2}$ absorber detected during observations 1, 3, 4, and 5–8 is associated with the torus at distances of $R_c^{\text{TOR}} = 0.14\text{--}5 \text{ pc}$ from the central black hole. On the other hand absorber is variable on long timescales (≥ 7 months), as shown by the lower column density during the 2010/04 *Chandra* observation 5–8. Such variability implies that the torus is clumpy rather than homogeneous, an important X-ray-only result which confirms previous indications for the clumpiness of the parsec-scale obscuring torus obtained in the IR (e.g. Ramos Almeida et al. 2011).

The column density of the individual clouds of the clumpy torus (say the observed mean of $\sim 4 \times 10^{22} \text{ cm}^{-2}$) can also be used to estimate the critical LOS with inclination i_{crit} that separates dust-free and dust-rich regions. Assuming the formalism of Liu & Zhang (2011), the critical LOS depends on the Eddington ratio (~ 0.036 for ESO 323–G77) and on the radiation pressure boost factor for dusty gas A (i.e. the ratio of the absorption cross section for dusty gas to that for electrons alone). For the given Eddington ratio, and for clouds with $N_{\text{H}} \sim 4 \times 10^{22} \text{ cm}^{-2}$, $A \sim 20$ (Fabian, Vasudevan & Gandhi 2008) so that $i_{\text{crit}} \sim 47^\circ$ (see Eq. 3 of Liu & Zhang 2011). We then conclude that the half-opening angle of the clumpy, dusty torus in ESO 323–G77 is of the order of $i_{\text{crit}} \sim 47^\circ$ in line with our expectation that our LOS (likely at $i \sim 45^\circ$) grazes the torus and intercept its atmosphere. Higher (lower) Eddington ratio AGN with torii having clumps of similar column density have larger (smaller) half-opening angles.

6.2 The $10^{23} - 10^{24} \text{ cm}^{-2}$ absorber during observations 2, 9, and 10

We now focus on the more absorbed states observed on 2006/06 (observation 2), 2011/07 (observation 9), and 2013/01 (observation 10) where column densities of $5.0 \pm 1.8 \times 10^{23} \text{ cm}^{-2}$, $1.5_{-0.6}^{+1.5} \times 10^{24} \text{ cm}^{-2}$, and $6.0 \pm 0.7 \times 10^{23} \text{ cm}^{-2}$ respectively are measured, see Fig. 9. As discussed in Section 3.2 (see Fig. 5), no absorption variability is detected during the *XMM-Newton* observation 10, so that $\Delta T_{\text{const}} \geq 1.2 \times 10^5 \text{ s}$. On the other hand, the sudden increase in column density during observation 2 can also be associated with a $10^{23} - 10^{24} \text{ cm}^{-2}$ absorber which is superimposed to the clumpy torus absorber discussed in the previous section (see Fig. 9). From

Table 3. The derived properties of the absorbing clouds in the different observations, together with their subsequent identification.

Cloud properties	Obs. 1, 3, 4, 5–8	Obs. 2, 9, 10
$N_{\text{H}} [\text{cm}^{-2}]$	$2 - 6 \times 10^{22}$	$0.3 - 3 \times 10^{24}$
$D_c [\text{cm}]$	$\geq 3.5 \times 10^{14}$	$0.9 - 50 \times 10^{14}$
$n_c [\text{cm}^{-3}]$	$\leq 1.7 \times 10^8$	$0.1 - 8 \times 10^9$
$v_c [\text{km s}^{-1}]$	150 – 900	900 – 3000
Origin	Clumpy TORUS	BLR

this event, one has that ΔT_{const} cannot be larger than the time-interval between observations 1 and 3, i.e. $\Delta T_{\text{const}} \leq 6.3$ months.

Using again Eq. 1, we then have that $D_c^{\text{TOR}} = 0.8 - 14 \times 10^{14} \text{ cm}$, $D_c^{\text{BLR}} = 0.9 - 50 \times 10^{14} \text{ cm}$, and $D_c^{\text{WIND}} = 0.2 - 70 \times 10^{15} \text{ cm}$ which, when combined with the observed common range of column densities in observations 2 and 10 ($5.3 - 6.7 \times 10^{23} \text{ cm}^{-2}$) imply that $n_c^{\text{TOR}} = 0.4 - 8 \times 10^9 \text{ cm}^{-3}$, $n_c^{\text{BLR}} = 0.1 - 8 \times 10^9 \text{ cm}^{-3}$, and $n_c^{\text{WIND}} = 0.008 - 3 \times 10^9 \text{ cm}^{-3}$.

The derived range of n_c^{TOR} is inconsistent with the upper limit derived in the previous section ($n_c^{\text{TOR}} \leq 1.7 \times 10^8 \text{ cm}^{-3}$) so that we can exclude that the clumpy torus is responsible for the absorption events with column density of $10^{23} - 10^{24} \text{ cm}^{-2}$, unless a very wide range of cloud properties is assumed for the same LOS. On the other hand, n_c^{BLR} is consistent with the number density needed to produce the optical and UV broad emission lines in the BLR, so that an identification of the absorber with a BLR cloud is totally plausible.

As for the wind, the upper limit on n_c^{WIND} may be marginally consistent with the expected wind density. However, some further constraints can be derived from the fact that our spectral analysis reveals absorption by neutral, rather than ionized gas. In fact, if we replace the neutral absorber of our spectral analysis by a ionized one, we have that $\log \xi \leq 1.3$. If we consider the densest possible wind-cloud ($n_c^{\text{WIND}} = 3 \times 10^9 \text{ cm}^{-3}$) together with the upper limit on the ionization parameter, then the wind must be located at $R_c^{\text{WIND}} \geq 2.7 \times 10^{16} \text{ cm}$ or $\geq 7.3 \times 10^{13} r_g$. Hence, we can exclude that we are seeing absorption by an inner disc-wind at the launching radii. On the other hand, the wind may participate to the observed absorption variability once it reaches much larger distances, that are typical of the BLR. In this framework, however, the wind and BLR are indistinguishable.

We conclude that the variable absorber with column density of $10^{23} - 10^{24} \text{ cm}^{-2}$ observed during observations 2, 9 and 10 is consistent with a BLR origin. The properties of the variable absorber(s) that we estimate from our analysis are reported in Table 3. We remind here that the only important assumptions we have made are (i) that the X-ray source has size of $D_s = 20 r_g$, and (ii) that the individual clouds have velocities appropriate to be associated with the torus, the BLR, or a disc-wind launched off the innermost few hundreds r_g .

6.3 Optical and UV simultaneous data from the *XMM-Newton* OM

According to our interpretation of the two *XMM-Newton* observations, the 2006/02 observation 1 is only absorbed by the clumpy torus, while the 2013/01 observation 10 is absorbed by (or additionally absorbed by) the BLR. In general, BLR clouds are not expected

Table 4. Flux densities in the UVW2, UVM2, and UVW1 OM filters during the *XMM–Newton* observations 1 and 10 are given in units of 10^{-15} erg cm $^{-2}$ s $^{-1}$ Å $^{-1}$.

OM filter	$f_{\text{obs.1}}^{\text{UV}}$	$f_{\text{obs.10}}^{\text{UV}}$
UVW2	1.5 ± 0.1	1.8 ± 0.1
UVM2	1.6 ± 0.1	2.3 ± 0.1
UVW1	4.4 ± 0.2	5.2 ± 0.3

to induce absorption variability in the UV as (i) the BLR are most likely dust-free, and (ii) even if they were dusty (at least partially, see e.g. Czerny & Hryniewicz 2011) their small size with respect to the UV-emitting region implies that they cannot imprint strong UV absorption variability, as they always cover globally the same fraction of the UV-emitting region. Hence, if observation 10 is indeed absorbed by the BLR cloud, no strong UV variability is expected between the two observations. Conversely, if the large column density during observation 10 occurs in the clumpy, dusty torus one may expect a lower UV flux during observation 10 than during observation 1. Although we have already excluded that this is the case, our result can be checked by looking for UV variability between observations 1 and 10.

We derive the UV flux densities in the *XMM–Newton* OM filters W2 (2120Å), M2 (2310Å), and W1 (2910Å) for both observations (filters V and U where used in addition during observation 1 and 10 respectively, so that they cannot be compared). Our results are reported in Table 4. As clear from the table, the UV fluxes during the more absorbed observation 10 are slightly higher than those during the less absorbed observation 1. Intrinsic flux variability cannot play a significant role, as the X-ray luminosity is in fact lower during observation 10 (see Table 2). This rules out that the $\sim 6 \times 10^{23}$ cm $^{-2}$ column density detected during observation 10 is due to a dusty extended medium (e.g. the clumpy torus) which affects the UV-emitting region of the disc, and strongly supports our interpretation in terms of BLR absorption.

7 CLUMPY ABSORBERS IN AGN: COMPARISON WITH PREVIOUS STUDIES

Clumpy X-ray absorbers have been previously detected in other AGN via X-ray absorption variability studies. In general, short-timescale absorption variability events have been associated with compact absorbers at the BLR scale, while (rarer) long-timescale events have been attributed to more extended absorbers such as the clumpy torus. Here we briefly compare our results on ESO 323–G77 with some of previous ones.

Clumpy torus absorption: Rivers, Markowitz & Rothschild (2011) report the detection of an X-ray eclipse in Cen A whose properties are consistent with the transit of one cloud with column density $\sim 4 \times 10^{22}$ cm $^{-2}$ into the LOS over the course of ~ 5.7 months. They were able to estimate a cloud linear size of $1.4 - 2.4 \times 10^{15}$ cm and a central number density of $1.8 - 3.0 \times 10^7$ cm $^{-3}$, in good agreement with previous results on the same source (Rothschild et al. 2011). The properties of the absorber imply an absorption event associated with the clumpy torus and are consistent with those we derive in ESO 323–G77. This is true for the observed column density of the individual clouds, as well as for their size and number density (see Table 3). This

strongly favours models in which the torus is made of individual clumps of column density of few $\times 10^{22}$ cm $^{-2}$ and number density of the order of few $\times 10^7$ cm $^{-3}$, as suggested by theoretical models (e.g. Nenkova et al. 2008a, 2008b).

BLR: X-ray absorption variability on much shorter timescales has been also reported in a number of sources. The most remarkable case is that of the Seyfert 1.8 galaxy NGC 1365 which shows common, multiple, and very rapid absorption variability events on timescales as short as a few hours (Risaliti et al. 2005; 2007; 2009). Adequate monitoring of these events allowed Risaliti et al. (2007) to constrain the X-ray continuum source size to $20 r_g$ at most (Risaliti et al. 2007; 2009), and to infer that absorption occurs in clouds with density of the order of 10^{10} cm $^{-3}$, size of few r_g , and velocity typical of the BLR. Further studies on the same source allowed to study the structure of the absorber in great detail, and Maiolino et al. (2010) conclude that the clouds have a strongly elongated and cometary shape, with a dense head, and an expanding, dissolving tail. The cometary tail inferred in NGC 1365 may well be a general property of the BLR clouds. As for ESO 323–G77, the cometary tail could be related to the highly ionized absorbers we detect, although the lower quality of our data with respect to those used by Maiolino et al. (2010) prevents us from performing further tests of this hypothesis. Other examples of X-ray absorption by clouds that are consistent with a BLR origin include Mrk 766 (Risaliti et al. 2011), where clouds with column density of few $\times 10^{23}$ cm $^{-2}$, density of $10^{10} - 10^{11}$ cm $^{-3}$, and linear size of $5 - 50 r_g$ are inferred, and SWIFT J2127.4+5654 (Sanfrutos et al. 2013) where the absorbing cloud has a lower column density of few $\times 10^{22}$ cm $^{-2}$, a density of $\geq 1.5 \times 10^9$ cm $^{-3}$ and a linear size of few r_g . In the latter case, the X-ray coverage of a full partial X-ray eclipse allowed Sanfrutos et al. (2013) to also estimate the X-ray continuum source linear size to be $\leq 10.5 r_g$. The BLR cloud(s) properties we estimate in ESO 323–G77 are consistent with the above results (see Table 3), although the slightly lower number density we obtain may indicate that absorption in ESO 323–G77 occurs in the outer BLR, closer to the dust sublimation radius than in NGC 1365 or Mrk 766. In summary, X-ray absorption variability on short-timescales points towards the presence of a compact (few r_g) X-ray continuum source that can be transiently obscured by clouds associated with the BLR.

Variable absorption in polar-scattered AGN: Finally, it is worth mentioning that X-ray absorption variability on a variety of timescales has been reported in a number of other polar-scattered AGN such as NGC 3227 (Lamer et al. 2003), Mrk 1239 (Grupe & Mathur 2004), Mrk 704 (Matt et al. 2011), Mrk 766 (Risaliti et al. 2011), and Mrk 231 (Piconcelli et al. 2013). Preliminary analysis reveals that absorption variability is also present in the polar-scattered Seyfert 1 galaxies Fairall 51 and (although somewhat marginally) NGC 4593 (Miniutti et al. in preparation; see also Jiménez-Bailón et al. 2008b). The large number of polar-scattered Seyfert 1 galaxies showing X-ray absorption variability (7 out of the 12 polar-scattered Seyfert 1 galaxies defined in the sample by Smith et al. 2004) strongly suggests that intermediate-inclination LOS of $40^\circ - 50^\circ$ are highly likely to give rise to X-ray absorption variability either due to clouds in clumpy torus or to BLR clouds, which may be out of the LOS for significantly less inclined LOS.

8 SUMMARY AND CONCLUSIONS

We report results from 10 X-ray observations of the polar-scattered Seyfert 1 galaxy ESO 323–G77 performed in the 2006–2013 time frame. The source exhibits remarkable X-ray spectral variability that is unambiguously associated with the variation of the column density of a neutral absorber towards the nuclear continuum. Our multi-epoch spectral analysis of ESO 323–G77 allows us to identify X-ray absorption by a clumpy torus, by BLR clouds, and by a warm/hot outflowing medium. The properties of the absorbers can be summarised as follows:

(i) **Clumpy torus:** the clumpy torus is responsible for X-ray absorption with column density of the order of $2-6 \times 10^{22} \text{ cm}^{-2}$. The torus clumpiness is demonstrated by the X-ray absorption variability on timescales shorter than 3.6 yr and longer than a few months. Our data enable us to infer that the typical size of the clumpy torus clouds is $D_c^{\text{TOR}} \geq 3.5 \times 10^{14} \text{ cm}$ with a typical number density $n_c^{\text{TOR}} \leq 1.7 \times 10^8 \text{ cm}^{-3}$. By combining the observed clumps column density with the radiation pressure boost factor for dusty gas, we estimate a torus half-opening angle of $\sim 47^\circ$. Although we are likely probing only the torus atmosphere with our X-ray observations, it is worth mentioning that if the cloud properties that we infer are representative of the typical clumpy torus cloud, a relatively large number $N_c \geq 15$ of clouds is required to be present in the equatorial plane to account for Compton-thick Seyfert 2 galaxies seen at nearly edge-on inclinations.

(ii) **BLR clouds:** BLR clouds are instead responsible for X-ray absorption with column density of the order of $0.3 - 3.0 \times 10^{24} \text{ cm}^{-2}$. The X-ray variability can be used to infer a typical BLR cloud size $D_c^{\text{BLR}} = 0.9 - 50 \times 10^{14} \text{ cm}$ with a typical number density $n_c^{\text{BLR}} = 0.1 - 8 \times 10^9 \text{ cm}^{-3}$, in line with the density that is needed to efficiently produce the optical/UV broad emission lines. The derived number density is slightly lower than that inferred from occultation events in e.g. NGC 1365 and Mrk 766 (e.g. Risaliti et al. 2009; 2011) and may imply that absorption in ESO 323–G77 occurs in the outer BLR, closer to the dust sublimation radius than in NGC 1365 and Mrk 766.

(iii) **Highly-ionized outflow:** we confirm the previous detection of a system of outflowing highly-ionized absorbers. The outflow velocity is of the order of $1000 - 4000 \text{ km s}^{-1}$, of the same order of the optical broad lines FWHM (2500 km s^{-1}). If the outflow velocity is comparable to the Keplerian velocity at the launching radius (notice that the escape velocity is just a factor $\sqrt{2}$ of larger than the Keplerian), the wind is then consistent with being roughly co-spatial with the BLR. Therefore, it is tempting to identify the outflowing gas with the inter-cloud medium that provides the pressure confinement for the colder BLR clouds. The lack of significant variability of the warm absorbers may indicate a clumpy outflow whose warm/hot phase is nearly homogeneous, and whose clumps may be identified with the line-emitting cold, dense BLR clouds. The warm/hot phase may also be connected with the mass loss of the cold clumps, as suggested by the BLR cometary shape suggested by Maiolino et al. (2010) in the case of NGC 1365.

In summary, multi-epoch X-ray observations of ESO 323–G77 enable us to directly map the clumpy torus and BLR clouds in X-ray absorption. We use X-ray data to derive with good precision the main properties of the absorbers (such as the size and density of the individual clumps). A more continuous X-ray monitoring of ESO 323–G77 and similar sources will allow us to significantly refine the X-ray derived clumpy torus and BLR properties in the future. We also suggest an identification of the highly-ionized out-

flowing warm absorber in ESO 323–G77 with the smooth, likely homogeneous inter-cloud BLR medium which may provide the pressure confinement for the cold BLR clouds. Within this scenario, the BLR clouds would simply be the cold, dense clumps of the smoother warm/hot outflow.

ACKNOWLEDGEMENTS

GM thanks Pilar Esquej and Almudena Alonso-Herrero for useful discussions. This work is based on observations obtained with XMM-Newton, an ESA science mission with instruments and contributions directly funded by ESA Member States and NASA. This research has also made use of data and/or software provided by the High Energy Astrophysics Science Archive Research Center (HEASARC), which is a service of the Astrophysics Science Division at NASA/GSFC and the High Energy Astrophysics Division of the Smithsonian Astrophysical Observatory. We made use of data obtained from the Chandra Data Archive and the Chandra Source Catalogue, and software provided by the Chandra X-ray Center (CXC) and of data obtained from the Swift observatory. We also made use of data from the *Suzaku* observatory, a collaborative mission between the space agencies of Japan (JAXA) and the USA (NASA). BAG, GM, and MS thank the Spanish MINECO for support through the Spanish Plan Nacional de Astronomía y Astrofísica under grant AYA2010-21490-C02-02.

REFERENCES

- Alonso-Herrero A. et al., 2011, *ApJ*, 736, 82
 Antonucci R., 1993, *Annual Review of Astronomy & Astrophysics*, 31, 473
 Arnaud K. A., 1996, *Astronomical Data Analysis Software and Systems V*, 101, 17
 Bianchi S., Miniutti G., Fabian A. C., Iwasawa K. 2005, *MNRAS*, 360, 380
 Bianchi S., Guainazzi M., Chiaberge M. 2006, *A&A*, 448, 499
 Bianchi, S., & Guainazzi, M., Proc. of the conference: The Multicolored Landscape of Compact Objects and Their Explosive Origins, eds: L. Antonelli, G. Israel, L. Piersanti, A. Tornambe, L. Burderi, T. Di Salvo, F. Fiore, G. Matt, M. Menna, 2007, *AIP Conf. Proc.*, 924, 822
 Czerny B., Hryniewicz K. 2011, *A&A*, 525, L8
 Dai X. et al., 2010, *ApJ*, 709, 278
 Elitzur M., Shlosman I., 2006, *ApJ*, 648, L101
 Esquej P. et al., 2013, submitted to *ApJ*
 Fabian, A. C., Vasudevan, R. V., & Gandhi, P. 2008, *MNRAS*, 385, L43
 Fairall A. P., 1986, *MNRAS*, 218, 453
 Gehrels N. et al., 2004, *ApJ*, 611, 1005
 Grupe, D., Mathur, S., & Komossa, S. 2004, *AJ*, 127, 3161
 Guainazzi M., Bianchi S., 2007, *MNRAS*, 374, 1290
 Guainazzi M., La Parola V., Miniutti G., Segreto A., Longinotti A. L., 2012, *A&A*, 547, A31
 Güver T., Özel F. 2009, *MNRAS*, 400, 2050
 Hönig S. F., Kishimoto M., Gandhi P., Smette A., Asmus D., Duschl W., Polletta M., Weigelt G., 2010, *A&A*, 515, A23
 Iwasawa K., Wilson A. S., Fabian A. C., Young A. J., 2003, *MNRAS*, 345, 369
 Jansen F. et al., 2001, *A&A*, 365, L1

- Jiménez-Bailón E., Krongold Y., Bianchi S., Matt G., Santos-Lleó M., Piconcelli E., Scharrel N., 2008a, MNRAS, 391, 1359
- Jiménez-Bailón E., Guainazzi M., Matt G., Bianchi S., Krongold Y., Piconcelli E., Santos Lleó M., Scharrel N., Proc. of the conference *The Nuclear Region, Host Galaxy and Environment of Active Galaxies*, eds: E. Benítez, I. Cruz-González, Y. Krongold, 2008b, Revista Mexicana de Astronomía y Astrofísica Conference Series, 32, 131
- Kalberla P. M. W., Burton W. B., Hartmann D., Arnal E. M., Bajaja E., Morras R., Pöppel W. G. L., 2005, A&A, 440, 775
- Lamer G., Uttley P., McHardy I. M. 2003, MNRAS, 342, L41
- Liu, Y., & Zhang, S. N. 2011, ApJ, 728, L44
- Maiolino R. et al., 2001, A&A, 365, 28
- Maiolino R. et al., 2010, A&A, 517, A47
- Matt G. et al., 2011, A&A, 533, A1
- Miller L., Turner T. J., Reeves J. N., Braitto V., 2010, MNRAS, 408, 1928
- Mitsuda K. et al., 2007, PASJ, 59, 1
- Mosquera A. M., Kochanek C. S., Chen B., Dai X., Blackburne J. A., Chartas G., 2013, ApJ, 769, 53
- Murphy K. D., Yaqoob T., 2009, MNRAS, 397, 1549
- Nandra K., O'Neill P. M., George I. M., Reeves J. N., 2007, MNRAS, 382, 194
- Nenkova M., Ivezić Ž., Elitzur M., 2002, ApJ, 570, L9
- Nenkova M., Sirocky M. M., Ivezić Ž., Elitzur M., 2008a, ApJ, 685, 147
- Nenkova M., Sirocky M. M., Nikutta R., Ivezić Ž., Elitzur M., 2008b, ApJ, 685, 160
- Nomura M., Ohsuga K., Wada K., Susa H., Misawa T., 2013, PASJ, 65, 40
- Piconcelli E., Bianchi S., Guainazzi M., Fiore F., Chiaberge, M., 2007, A&A, 466, 855
- Piconcelli E., Miniutti G., Ranalli P., Fiore F., Maiolino R., 2013, MNRAS, 428, 1185
- Poncellet A., Perrin G., Sol H. 2006, A&A, 450, 483
- Ramos Almeida C., et al., 2011, MNRAS, 417, L46
- Ranalli P., Comastri A., Setti G., 2003, A&A, 399, 39
- Reeves J. et al., 2008, MNRAS, 385, L108
- Risaliti G., Elvis M., Fabbiano G., Baldi A., Zezas A., 2005, ApJ, 623, L93
- Risaliti G., Elvis M., Fabbiano G., Baldi A., Zezas A., Salvati M., 2007, ApJ, 659, L111
- Risaliti G. et al., 2009, ApJ, 696, 160
- Risaliti G., Elvis M., 2010, A&A, 516, A89
- Risaliti G., Nardini E., Salvati M., Elvis M., Fabbiano G., Maiolino R., Pietrini P., Torricelli-Ciamponi G., 2011, MNRAS, 410, 1027
- Rivers E., Markowitz A., Rothschild R., 2011, ApJ, 742, L29
- Ross R. R., Fabian A. C., 2005, MNRAS, 358, 211
- Rothschild R. E., Markowitz A., Rivers E., Suchy S., Pottschmidt K., Kadler M., Müller C., Wilms J., 2011, ApJ, 733, 23
- Sanfrutos M., Miniutti G., Agís-González B., Fabian A. C., Miller J. M., Panessa F., Zoghbi A., 2013, MNRAS in press (preprint: arXiv:1309.1092)
- Schmid H. M., Appenzeller I., Camenzind M., Dietrich M., Heidt J., Schild H., Wagner S., 2001, A&A, 372, 59
- Schmid H. M., Appenzeller I., Burch U., 2003, A&A, 404, 505
- Smith P. S., Schmidt G. D., Allen R. G., Angel J. R. P., 1995, ApJ, 444, 146
- Smith R.K., Brickhouse N.S., Liedahl D.A., Raymond J.C., 2001, ApJ, 556, L91
- Smith J. E., Robinson A., Alexander D. M., Young S., Axon D. J., Corbett E. A., 2004, MNRAS, 350, 140
- Tatum M. M., Turner T. J., Sim S. A., Miller L., Reeves J. N., Patrick A. R., Long K. S., 2012, ApJ, 752, 94
- Tombesi F., Cappi, M., Reeves J. N., Palumbo G. G. C., Yaqoob T., Braitto V., Dadina, M., 2010, A&A, 521, A57
- Tombesi F., Cappi M., Reeves J. N., Braitto V., 2012, MNRAS, 422, L1
- Tristram K. R. W., Meisenheimer K., Jaffe W., et al., 2007, A&A, 474, 837
- Turner T. J., Miller L., A&A Rev., 2009, , 17, 47
- Vasudevan, R. V., & Fabian, A. C. 2007, MNRAS, 381, 1235
- Wang, J.-M., & Zhang, E.-P. 2007, ApJ, 660, 1072
- Weisskopf M. C., Tananbaum H. D., Van Speybroeck L. P., O'Dell S. L., 2000, Proc. SPIE, 4012, 2
- Winkler H., 1992, MNRAS, 257, 677
- Winkler H., Glass I. S., van Wyk F., Marang F., Jones J. H. S., Buckley D. A. H., Sekiguchi K., 1992, MNRAS, 257, 659
- Yaqoob, T. 2012, MNRAS, 423, 3360